JOURNAL OF SYNCHROTRON RADIATION
ISSN 1600-5775

Investigation of (micro-)meteoritic materials at the new hard X-ray imaging PUMA beamline for heritage sciences

Pieter Tack,[a]* Benjamin Bazi,[a] Bart Vekemans,[a] Tulin Okbinoglu,[b] Flore Van Maldeghem,[c] Steven Goderis,[c] Sebastian Schöder[b] and Laszlo Vincze[a]

[a]Chemistry, Ghent University, Krijgslaan 281 S12, 9000 Ghent, Belgium, [b]PUMA beamline, Synchrotron SOLEIL, Saint-Aubin BP48, F-91192 Gif-sur-Yvette, France, and [c]Analytical-, Environmental- and Geo-chemistry, Vrije Universiteit Brussel, Pleinlaan 2, 1000 Brussels, Belgium. *Correspondence e-mail: pieter.tack@ugent.be

Received 22 May 2019
Accepted 4 September 2019

Edited by S. Svensson, Uppsala University, Sweden

Keywords: PUMA; confocal XRF; XANES; differential imaging; cultural heritage; micrometeorite; pallasite.

Supporting information: this article has supporting information at journals.iucr.org/s

At the French synchrotron facility SOLEIL, a new X-ray imaging facility PUMA (Photons Utilisés pour les Matériaux Anciens) has been made available to scientific communities studying materials from cultural heritage. This new instrument aims to achieve 2D and 3D imaging with microscopic resolution, applying different analytical techniques including X-ray fluorescence spectroscopy (XRF), X-ray absorption spectroscopy (XAS), X-ray diffraction and phase-contrast imaging. In order to discover its capabilities a detailed analytical characterization of this beamline as an analytical and imaging tool is deemed necessary. In this work, (confocal) XRF and XAS analyses are demonstrated using the Seymchan pallasite meteorite and an Antarctic unmelted micrometeorite as case studies. The obtained spatial resolution (2 μm × 3 μm) and sensitivity (detection limits <10 p.p.m. for 1 s acquisition at 18 keV) show that PUMA is a competitive state-of-the-art beamline, providing several high-profile and high-in-demand analytical methods while maintaining applicability towards a wide range of heritage-oriented sciences.

1. Introduction

Investigation using X-ray based methods (on the microscopic scale) of ancient materials, *e.g.* in the fields of archaeology, palaeontology, paleo-environmental and conservation sciences, is usually performed at synchrotron radiation facilities owing to the non-destructive character of the analyses (Bertrand *et al.*, 2012; Schalm *et al.*, 2016; Grieten *et al.*, 2017; Brun *et al.*, 2016; Tack *et al.*, 2016; Monico *et al.*, 2015; Alfeld *et al.*, 2010; Vanmeert *et al.*, 2015; Salomé *et al.*, 2013; Fayard *et al.*, 2013; De Pauw *et al.*, 2018). However, access to these facilities is often limited. Furthermore, ancient materials research often has to compete for beam time with other research fields and regularly requires the investigation of complete sets or large sample series, requiring significant amounts of beam time. For this purpose, a new beamline has been constructed at the SOLEIL synchrotron (Gif-sur-Yvette, France) dedicated to the investigation of ancient materials, and developed in collaboration with the IPANEMA platform (Institut Photonique d'Analyse Non-destructive Européen des Matériaux Anciens; Bertrand *et al.*, 2011). The PUMA (Photons Utilisés pour les Matériaux Anciens) beamline is a hard X-ray imaging beamline optimized for the scientific communities of the heritage sciences and allows for 2D and 3D imaging capabilities with a microscopic spatial resolution, applying several analytical techniques including X-ray fluorescence spectroscopy (XRF), X-ray absorption spectroscopy (XAS), X-ray diffraction (XRD) and phase-contrast imaging.

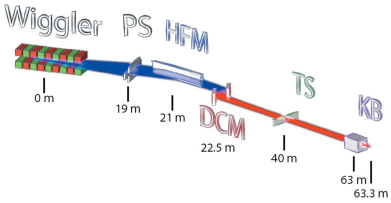

At the time of the experiment, the latter two techniques' measurement environments were still under construction, and as such no further information about them is provided in this report.

Several of these methods have been applied to investigate a set of (micro-)meteorites, preceded by full characterization of the PUMA beamline properties. We opted to investigate a set of (micro-)meteorites that may challenge the capabilities and show the limits of the PUMA instrument, extracting 2D/3D microscopic information of such heterogeneous samples. Planetary materials are often very old (typically 4.6 billion years old, with presolar grains inherited from even older stellar environments), vary widely in size (from km-sized impact crater-forming projectiles to micrometric dust), are relatively simple in terms of composing phases (*e.g.* Fe/Ni metals versus silicate minerals) and can be extremely rare (*e.g.* unique achondrites). As such, they are suited perfectly as test samples for the PUMA beamline, specialized in the investigation of ancient, rare and cultural heritage materials. The samples investigated here are (i) a fragment of the Seymchan pallasite and (ii) an Antarctic unmelted micrometeorite.

Pallasites are stony-iron meteorites consisting of easily recognisable olivine and minor phases such as troilite, chromite, schreibersite, pyroxene, phosphates and phosphoran olivine, within an iron–nickel metal matrix (Boesenberg *et al.*, 2012). As such, pallasites are thought to represent mixtures of planetesimal core and mantle materials, although the formation processes and nature of the sampled planetary reservoirs remain a topic of scientific debate (Tarduno *et al.*, 2012).

The Seymchan meteorite is a pallasite recovered from the Seymchan area in Russia and belongs to PMG-am (pallasite 'main group' – anamolous metal) pallasite subtype, and is also characterized by abundant (percentage level by area) and large (up to 0.5 cm in length) heterogeneously distributed chromites (van Niekerk *et al.*, 2007; Wasson & Choi, 2003). Chromites, showing large chemical variation, may represent a key tracer of the crystallization history of pallasites given their limited mineralogical diversity (Boesenberg *et al.*, 2018).

Compared with the relatively large phases composing pallasites, micrometeorites are tiny dust particles between 10 µm and 2 mm in size that dominate approximately 40 000 metric tons of extra-terrestrial matter accreting to Earth every year (Love & Brownlee, 1993; Rubin & Grossman, 2010). These microscopic particles are thought to sample parent bodies different from those of meteorites and are derived from not only asteroidal but possibly also from cometary sources (Rubin, 2018). For over 10 years, micrometeorites have been recovered from micrometeorite-rich erosional and eolian sediment collected near high-altitude Antarctic mountain summits (>1650 masl), including those in the Transantarctic and Sør Rondane mountain ranges (Goderis *et al.*, 2019; Rochette *et al.*, 2008). The micrometeorites recovered from these sites are commonly larger than those from other collection sites and occur at relatively high concentrations, yet even these size ranges (>100 µm) still limit the application of many analytical techniques (Rochette *et al.*, 2008; Suavet *et al.*, 2009).

Primary meteorite components, including chondrules and Ca–Al-rich inclusions and relict minerals such as olivine and Mg–Al spinel, can be sampled by unmelted micrometeorites. These phases often contain crucial information on the initial nature of the micrometeorite precursor and the thermal history experienced by the particle. Elemental compositions in conjunction with oxygen isotope ratio measurements (Noguchi *et al.*, 2002; Genge *et al.*, 1997) can be used to further classify micrometeorites into various meteorite clans and groups (Meteoritical Bulletin Database, https://www.lpi.usra.edu/meteor/; Folco & Cordier, 2015).

2. Materials and methods

2.1. Beamline description

The PUMA beamline (Fig. 1) uses X-rays generated by a 1.8 T wiggler insertion device, originating from a 8 µm (V) × 188 µm (H) electron beam source size. The wiggler consists of 20 periods of 164.2 mm period length, uses a fixed gap at 14.5 mm and is characterized by a critical energy of approximately 8.98 keV. An elliptical horizontal deflection mirror with a 600 Å Ir coating mounted in a fixed 1.3 mrad angle with adjustable bending provides a high reflectivity in the entire energy range (4–60 keV), and can be used for pre-focusing of the beam in the horizontal direction. An Si(111) double-crystal monochromator (DCM) was used to obtain a monochromatic photon beam with an energy resolution ($\Delta E/E$) of approximately 2×10^{-4}.

To further focus the beam, apart from the pre-focusing of the elliptical horizontal deflection mirror, a Kirkpatrick–Baez (KB) mirror system was used. The KB mirror contains a 60 nm Rh stripe, which also aids in higher-order harmonic rejection originating from the DCM. To reduce relative movements between KB and the sample position, both are mounted on the same granite block. An optimal spot size at the sample position of 2 µm (V) × 3 µm (H) was obtained using an 18 keV X-ray beam.

Samples, typically fixed on brass pins (3.15 mm, Huber), are positioned in the X-ray beam using a motor assembly consisting of a set of stacked motors that can perform the

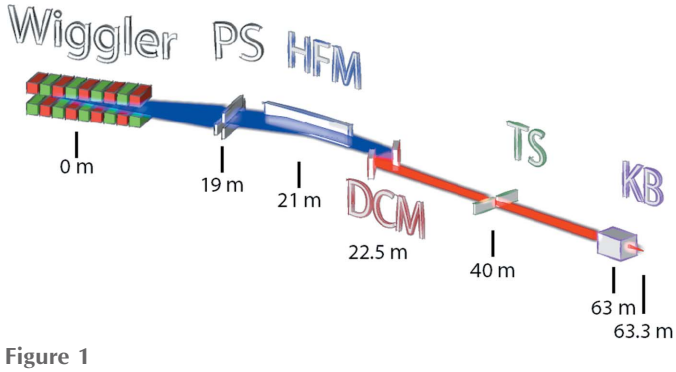

Figure 1
Schematic synoptic of the PUMA beamline with the distances of all elements to the source. The following abbreviations are used: PS – primary slits, HFM – horizontal focusing mirror, DCM – double-crystal monochromator, TS – tertiary slits, KB – Kirkpatrick–Baez mirror.

necessary sample movements for the different methods applied: (i) two long translation stages to move the sample along the path of the beam, changing the distance between the sample and focusing optics, and perpendicular to this, (ii) a fast scanning module mounted on top of a rotation stage, consisting of three translation stages with sub-micrometre precision, allowing the sample to translate in the vertical direction (z) and in the horizontal plane (x, y). In this experiment, the rotation stage was set to 45° to align the stages with the sample surface. Additionally, tilt stages (±5°) are present to improve the vertical alignment of the sample. An optical video microscope (Hamamatsu digital camera C11440) has been installed to monitor the sample position and assures its placement in the beam focal point. The microscope is equipped with a 10× magnification lens, providing a 700 µm × 700 µm field of view at a 28 mm working distance with 10 µm focal depth, assuring accurate positioning of the sample in the focal point of the X-ray beam. The long working distance allows sample observation during irradiation to monitor unexpected sample behaviour such as thermal drift or radiation damage.

2.2. XRF analysis

XRF measurements were performed using an excitation energy of 18 keV. Data were acquired using a Sirius-SD silicon drift detector (RaySpec Ltd) with a 100 mm^2 active area (on chip 80 mm^2 collimated), 450 µm-thick crystal and 25 µm-thick Be window. A cylindrically shaped aluminium collimator with 8 mm internal diameter and 10 mm length was used to reduce the spectral contribution of background scattering and unwanted signals from the sample environment. For confocal XRF measurements, an 8 cm-long polycapillary optic (XOS Inc.) with 2 mm focal distance, 1.5 mm outer diameter at the sample side and 7.5 mm outer diameter at the detector side was used.

The XRF spectra were calibrated and integrated using the *AXIL* software package (Vekemans *et al.*, 1994) before normalization for incident beam flux variations and detector dead time. Quantification was performed based on the use of geological reference materials (RM) with known compositions such as MPI-DING glasses, ATHO-G, GOR132-G, KL2-G and ML3B-G (Jochum *et al.*, 2000). An approximate elemental yield was determined for each certified element in the reference materials by dividing the XRF net peak intensity by the corresponding certified concentration, under the assumption that the density × thickness factor is identical for the samples and RM used. Where an element is present in multiple reference materials, the average elemental yield was used with its standard deviation as a measure of the resulting uncertainty. For elements that are not present in any of the reference materials used, the elemental yield was determined by interpolation of the closest neighbouring elements, by atomic number, that were present in the reference materials. Data obtained through the so-called *fly scan* routine, in which the sample is moved continuously through the beam at a given speed and spectra are acquired over set time intervals, were corrected for their encoder motor positions before visualization of the data.

Detection limits (DLs) were determined, following Beckhoff and co-workers, to be three times the square root of the background intensity, multiplied by the certified concentration and divided by the net peak intensity (Beckhoff *et al.*, 2007). DLs presented for a 1 s measurement time were obtained by multiplying the DLs corresponding to a 1000 s live time with the square root of 1000, based on considerations from Poisson statistics. Obtained uncertainties were calculated through error propagation of the certified concentration uncertainty, as well as taking into account the counting statistics uncertainty for the experimental data.

The beam size and confocal polycapillary acceptance were determined by performing translational scans over a 10 µm-diameter stainless-steel wire (Goodfellow) and monitoring the emitted Fe $K\alpha$ intensity. The resulting profile was fit using a Gaussian function, the full width at half-maximum of which was deconvoluted with the wire thickness (10 µm) to present the obtained beam size or polycapillary optic acceptance.

2.3. XANES analysis

Fe K-edge X-ray absorption near-edge structure (XANES) data were obtained according to the following scan routine: 7044.8–7104.8 eV in 3 eV steps, 7104.8–7134.8 eV in 0.3 eV steps and 7134.8–7264.8 eV in 3 eV steps. Depending on the signal intensity, multiple scans were repeated and averaged to improve data quality. All spectra were collected in emission mode and corrected for detector dead time. Spectra were normalized by performing a linear pre-edge background subtraction and normalizing the edge jump to 1 at 7162 eV ($E = E_0 + 50$ eV). At several occasions during the experiment, a reference sample (Fe_2O_3) was measured to check and correct for potential shifts in energy. During the experiment no such variations were observed.

In order to identify mineral phases, the experimental XANES spectra were compared with a set of spectra obtained from known, pure mineral phases. Those most important for this research include wüstite (FeO), hematite (α-Fe_2O_3), magnetite (Fe_3O_4), olivine [$(Mg^{2+},Fe^{2+})_2SiO_4$], iron chromite ($FeCr_2O_4$) and metallic iron. Linear combination fitting was performed to determine the relative contribution of each known phase to the unknown spectrum. The sum of all relative contributions was not set to 1 to add an additional degree of freedom and prevent the fitting algorithm to fit negative contributions.

3. Results

3.1. Beamline characterization

The primary X-ray beam divergence around the sample position of the PUMA beamline was investigated by determining the beam size, as described in the *Materials and methods* section, at 100 µm intervals over a range of 5 mm along the beam trajectory, for three different energies: 7.3 keV, 12.5 keV and 18 keV. Both vertical and horizontal

Table 1
Horizontal and vertical beam divergence as a function of primary beam photon energy.

Energy (keV)	7.3	12.5	18.0
Horizontal divergence (mrad)	0.40	1.90	0.50
Vertical divergency (mrad)	0.30	0.20	0.30

beam sizes were assessed. The obtained vertical beam sizes are displayed in Fig. 2, whereas the horizontal and vertical beam divergencies are displayed in Table 1. Results for the horizontal beam size at 12.5 keV deviate somewhat from the other obtained values due to the occurrence of beam splitting when placing the sample out of beam focus. This beam splitting was also perceived in the horizontal direction at different energies, but to a lesser degree relative to the bulk of the signal, so this effect did not interfere with the beam size determination algorithm. Overall, it can be stated that a horizontal beam divergence of approximately 0.5 mrad (H) × 0.3 mrad (V) was determined.

Given the size and nature of the reported samples and the available beam time, we opted to measure the samples in a position characterized by a 7 µm (H) × 2 µm (V) beam size at 18 keV, although it was found that a beam size down to 3 µm × 2 µm is achievable at the PUMA beamline at this energy. This sample position results in beam widening to 20 µm (H) × 17 µm (V) at 7.3 keV, which is the size of beam used for all subsequent XANES measurements.

Detection limit calculations were calculated for a sample-to-detector distance of 5 mm and in confocal mode where the view of the detector was limited to a microscopic volume using a polycapillary optic, as described in the *Materials and methods* section. Comprehensive tables of these detection limits and their respective uncertainties are included in the supporting information. A graphical representation of the results for samples with a geological (ATHO-G), biological (NIST 1577c bovine liver) and glass (ATHO-G, NIST 613) matrix are displayed in Fig. 3. In general, the detection limits for confocal measurements are slightly higher than that found in the near position: 1–200 p.p.m. versus 0.1–100 p.p.m. for a 1 s measurement time and atomic number between 17 and 83.

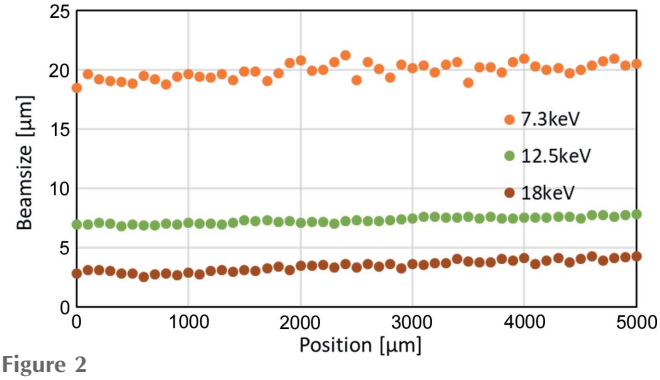

Figure 2
Vertical beam size as a function of sample position over a 5 mm range at 7.3 keV (orange dots), 12.5 keV (green triangles) and 18 keV (brown squares).

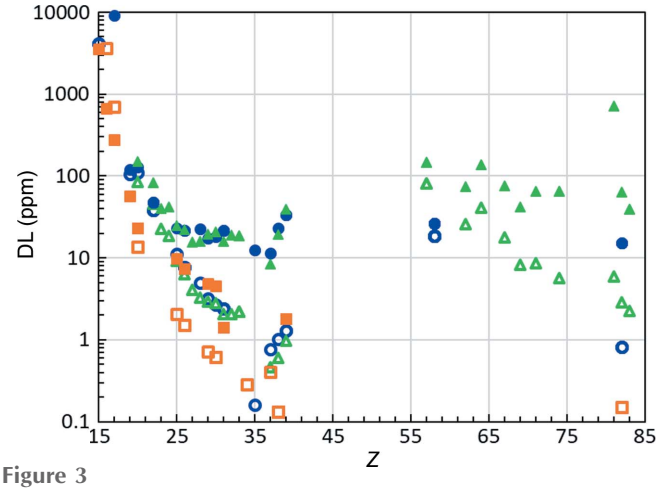

Figure 3
Detection limits as a function of atomic number Z for a 1 s acquisition live time at near (hollow marks) and confocal (filled marks) detection mode for ATHO-G (blue), NIST 1577c (orange) and NIST SRM 613 (green) for a 7 µm (H) × 2 µm (V) beam size at 18 keV.

For a 1000 s measurement time, sub-p.p.m. detection limits were obtained for the majority of elements reported here.

3.2. µXRF imaging

The Seymchan pallasite meteorite sample was analysed using µXRF spectroscopy with the *fly scan* approach. An area of 700 µm × 700 µm was covered in intervals of 5 µm × 2 µm at a rate of 0.2 s per interval. An overview of the measurement results can be seen in Fig. 4. Three distinct phases can be recognized: a Cr–Mn rich phase (top right), an Fe–Ni rich phase (centre diagonal) and a phase containing no Ni or Cr (bottom left).

The quantitative results display relative concentration levels of approximately 30 wt% and 10 wt% for Fe and Ni, respectively, in the Fe–Ni-rich phase; 5 wt% and 45 wt% for Fe and Cr, respectively, in the Cr-rich phase (chromite); and 10 wt% Fe in the Ni- and Cr-poor phase (olivine). Relative uncertainties of these results are in the range of several percent due to the semi-quantitative approach that was followed (see *Materials and methods* section).

These concentration values are in line with what is expected based on previous measurements. In contrast to the homogeneous nature of the chromite and olivine crystals, which show no zonation, Ni concentration gradients can be perceived within the Fe–Ni-rich phase, suggesting the presence of multiple Ni-rich Fe phases such as plessite, a fine-grained mixture of kamacite and taenite.

3.3. µXANES

XANES measurements were performed on the selected points from Fig. 4(*c*), corresponding to the various phases characterized (chromite, Fe–Ni metal, olivine; see Fig. 5). A slightly higher noise level was obtained than expected, based on the highly intense Fe XRF map. This is mainly due to the decrease in primary beam flux at energies around the Fe *K*-edge (7.112 keV) compared with what is obtained at 18 keV:

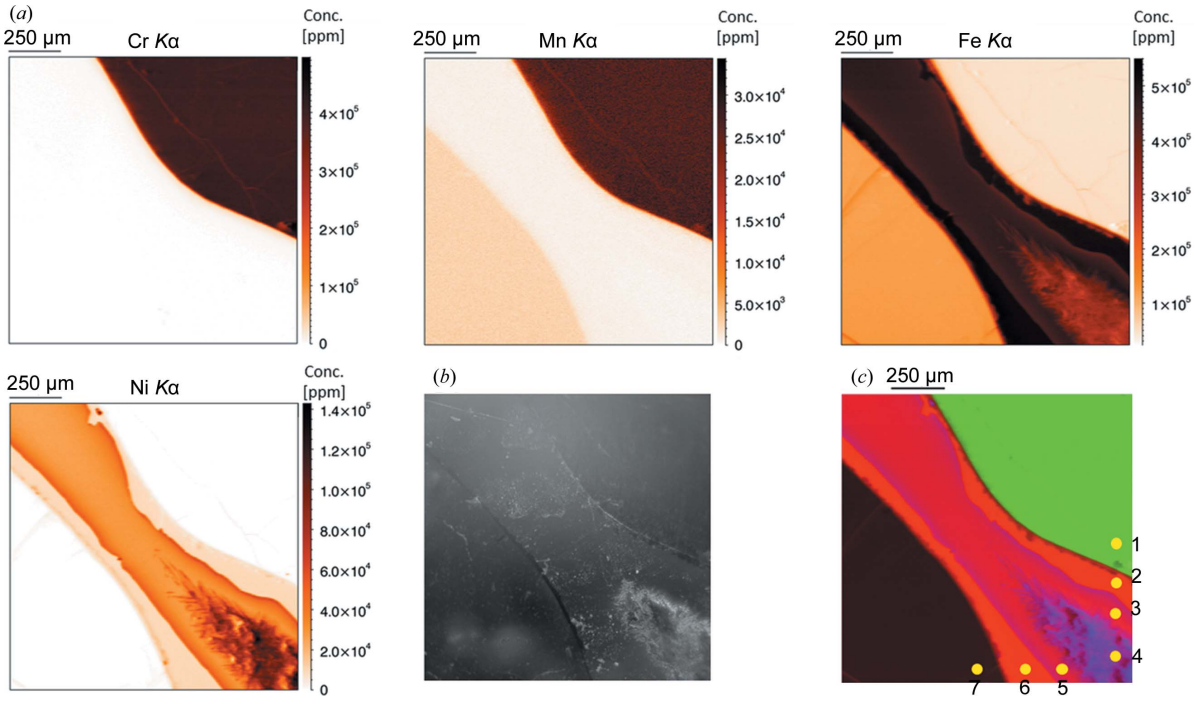

Figure 4
(*a*) XRF elemental distribution maps acquired from the Seymchan pallasite, (*b*) microscope image of the corresponding region as acquired at the beamline during the experiment and (*c*) RGB image of Fe (red), Ni (blue) and Cr (green) with yellow marks corresponding to the locations of the XANES measurements.

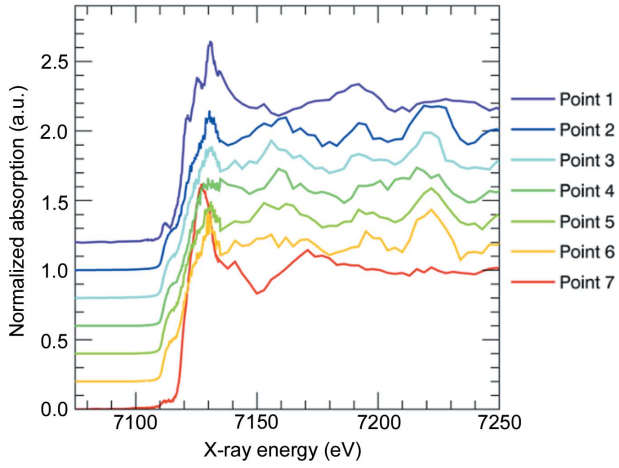

Figure 5
Fe *K*-edge XANES curves for the points selected in the Seymchan pallasite.

5.2×10^8 versus 1.5×10^{10} photons s^{-1}. Nevertheless, representable XANES profiles could be acquired within a 4 s measurement time per energy step.

Linear combination analysis shows that point 1 corresponds to an iron chromite phase, whereas the spectrum of point 7 matches that of olivine. Points 2–6 display similar XANES profiles that match with a metallic Fe phase. It should be noted that the profiles of points 2–6 are corrected for self-absorption effects: the XANES features were attenuated due to the high Fe concentration.

3.4. Differential imaging

Using the above-mentioned µXANES approach, three separate phases were identified within the field of view of this Seymchan sample. The drawback of this method is that one assumes that the selected points for XANES analysis are representative for the entire phase/region in which the points are included. This could lead to oversight of other certain phases that are not immediately visible from the XRF maps displayed in Fig. 4. As it would require a long measurement time to perform a full XANES measurement on each point (several weeks, applying the current measurement conditions; Tack *et al.*, 2014, 2017) or a large subset thereof, we opted to perform a so-called differential imaging approach.

In this method, XRF maps are acquired at set excitation energies along the XANES spectrum (Fig. 6). The different phases can then be visualized separate from the rest: in map 5 (E_0: 7.1148 keV) only the metallic phase is excited, and thus provides an XRF response. Differentiation between chromite and olivine is less straightforward as these phases do not display distinct energies at which only one of the two is (significantly more) excited. Nevertheless, olivine can be identified by division of map 4 (E_0: 7.1276 keV, at the olivine white line energy, *i.e.* olivine emits the most fluorescence) by map 2 (E_0: 7.150 keV, olivine emits less photons compared with the Fe–Ni metal and chromite). Similarly, chromite can be identified by division of map 3 (E_0: 7.1312 keV) by maps 2 and 1 (E_0: 7.265 keV). The resulting image, after correction for a small image shift (~3 µm per map), either through sample displacement or as a result of beam position shift as a function

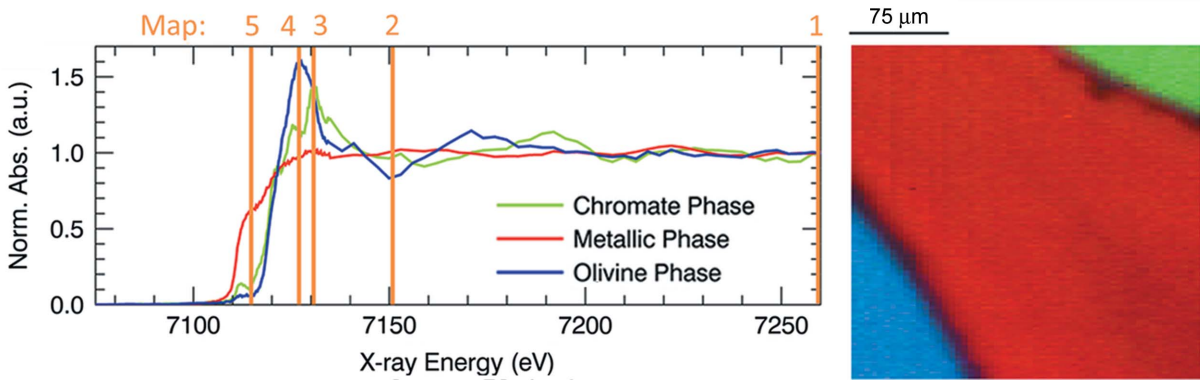

Figure 6
Left: Fe *K*-edge XANES of the different Seymchan pallasite phases with annotation of the excitation energies at which XRF maps were acquired for differential imaging. Right: RGB image displaying the result of the differential imaging, displaying three distinct phases: olivine (blue), metallic Fe–Ni (red) and chromite (green).

of energy, is displayed in the right panel of Fig. 6. From this image, it is clear that the points for XANES measurement were indeed representative for olivine and chromite. In addition, the metallic Fe phase shows that the Ni/Fe gradient is not linked to a shift in oxidation state of the Fe atoms. A vague shadowing is visible in the bottom right part of the metallic Fe phase (red), which could suggest a slightly different coordination, although this could also be due to residual concentration effects.

3.5. Confocal 3D µXRF

In order to display the 3D XRF capabilities at the PUMA beamline a confocal detection scheme was installed. A confocal volume of 2 µm (V) × 7 µm (H) × 15 µm (D) was obtained at 18 keV excitation energy and Fe *Kα* detection. A photograph of the setup with Antarctic micrometeorite UM1 (173 µm in diameter) in the confocal volume and an RGB XRF elemental distribution image determined for the centre slice of the sample are provided in Fig. 7. A full 3D XRF volume was acquired by scanning the particle through the confocal volume. The resulting 3D elemental distribution volume is provided in the supporting information. It is clear that the spatial resolution provided is sufficient to partially recognize the internal texture and porosity of the particle and identify encapsulated regions that are locally enriched in Fe (rim and interior), Cr, Ni or Ca (interior mostly) (see also video S1 of the supporting information). These enriched regions highlight the highly heterogeneous nature of this porous unmelted micrometeorite, confirming that this micrometeorite and similar microscopic particles mostly sample chondritic parent precursors, but do not reflect representative volumes of these bodies. This illustrates the control of mineral constituents (*e.g.* in the form of relict minerals or primary meteorite components) on the bulk chemical composition of micrometeorites in general. Combining these data for a subset of unmelted micrometeorites could provide crucial 3D information on the processes that lead to the formation of these particles and their subsequent modification following atmospheric entry, all in a non-destructive manner.

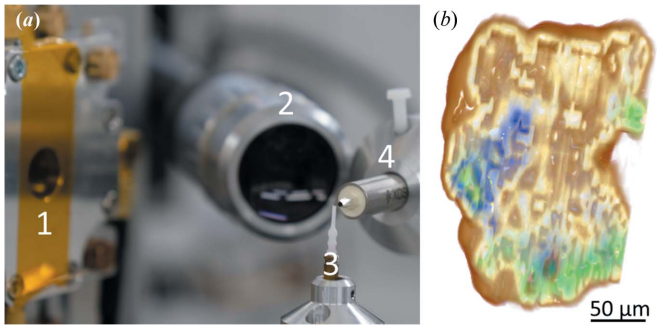

Figure 7
(*a*) Photograph of the sample environment at the PUMA beamline displaying (1) the KB-mirror exit window, (2) online sample microscope, (3) sample mount with the UM1 micrometeorite particle on a plastic holder tip and (4) detector with polycapillary optic. (*b*) XRF image of a slice through the particle displaying Fe (yellow–brown), Ni (red), Ca (green) and Cr (blue).

4. Conclusions

The PUMA beamline at SOLEIL is a new hard X-ray imaging beamline made available to science communities studying cultural heritage materials. PUMA allows for 2D and 3D imaging capabilities with a microscopic resolution, applying several analytical techniques including XRF, XAS, XRD and phase-contrast imaging. It generates photons using a 1.8 T wiggler insertion device with 8.98 keV critical energy. Using a KB-mirror optic, a beam size of 2 µm (V) × 3 µm (H) can be obtained with a photon flux of 1.5 × 10^{10} photons s^{-1} at 18 keV. Detection limits of 0.1–100 p.p.m. for a 1 s measurement time and elements with an atomic number between 17 and 83 were obtained for geological, biological and glass sample matrices.

Several analytical methods were demonstrated using the Seymchan pallasite meteorite and an unmelted micrometeorite as case studies: X-ray fluorescence micro-spectroscopy, µXANES, differential imaging, confocal XRF and 3D confocal imaging. The results obtained confirm the effectiveness of the PUMA beamline in characterizing the chemical

and mineralogical composition of microscopic particles and mineral phases in a non-destructive manner. Chemical heterogeneity within the studied meteoritic materials was traced at the micrometre-scale, whereas mineral phases were successfully detected and identified at a spatial resolution of ∼10 µm. Application of the selected analytical techniques to a larger set of similar materials (*e.g.* from asteroid or comet sample-return missions) could provide critical 2D and 3D information on the planetary processes that lead to the formation of these extra-terrestrial samples and their subsequent modification after atmospheric entry and during their residence at the Earth's surface.

Additionally, the obtained results with respect to the detection limit, spatial resolution and the availability of a multitude of analytical X-ray based techniques during a single measurement campaign display the usefulness of PUMA regarding non-destructive microscopic 2D/3D chemical and structural analysis for cultural heritage related materials, as these materials often entail samples with similar compositional matrices as the reference materials and meteoritic materials that were investigated during this experiment.

Acknowledgements

We wish to acknowledge SOLEIL for funding the beam time and for providing the synchrotron beam.

Funding information

The following funding is acknowledged: Fonds Wetenschappelijk Onderzoek (grant No. 1502819N to PT) Excellence of Science ET-HOME project (grant No. G099817N to SG); Belgian Federal Science Policy Office (grant No. BRAIN-be BAMM! to SG); VUB Strategic Research Council (grant No. AMGC to SG); UGent Bijzonder Onderzoeksfonds (Geconcerteerde Onderzoeksacties).

References

Alfeld, M., Janssens, K., Sasov, A., Liu, X., Kostenko, A., Rickers-Appel, K. & Falkenberg, G. (2010). *X-ray Opt. Microanal. Proc.* **1221**, 111–118.

Beckhoff, B., Kanngießer, B., Langhoff, N., Wedell, R. & Wolff, H. (2007). *Handbook of Practical X-ray Fluorescence Analysis*. Berlin, Heidelberg: Springer.

Bertrand, L., Cotte, M., Stampanoni, M., Thoury, M., Marone, F. & Schöder, S. (2012). *Phys. Rep.* **519**, 51–96.

Bertrand, L., Languille, M.-A., Cohen, S. X., Robinet, L., Gervais, C., Leroy, S., Bernard, D., Le Pennec, E., Josse, W., Doucet, J. & Schöder, S. (2011). *J. Synchrotron Rad.* **18**, 765–772.

Boesenberg, J. S., Delaney, J. S. & Hewins, R. H. (2012). *Geochim. Cosmochim. Acta*, **89**, 134–158.

Boesenberg, J. S., Humayun, M., Windmill, R., Greenwood, R. C. & Franchi, I. A. (2018). *Lunar Planet. Sci. Conf.* **49**, 1556.

Brun, E., Cotte, M., Wright, J., Ruat, M., Tack, P., Vincze, L., Ferrero, C., Delattre, D. & Mocella, V. (2016). *Proc. Natl Acad. Sci. USA*, **113**, 3751–3754.

De Pauw, E., Tack, P., Verhaeven, E., Bauters, S., Acke, L., Vekemans, B. & Vincze, L. (2018). *At. Spectrosc.* **149**, 190–196.

Fayard, B., Pouyet, E., Berruyer, G., Bugnazet, D., Cornu, C., Cotte, M., Andrade, V. D., Chiaro, F. D., Hignette, O., Kieffer, J., Martin, T., Papillon, E., Salomé, M. & Sole, V. A. (2013). *J. Phys. Conf. Ser.* **425**, 192001–192004.

Folco, L. & Cordier, C. (2015). *Planetary Mineralogy*, edited by M. R. Lee & H. Leroux, pp. 253–297. London: European Mineralogical Union and the Mineralogical Society.

Genge, M. J., Grady, M. M. & Hutchison, R. (1997). *Geochim. Cosmochim. Acta*, **61**, 5149–5162.

Goderis, S., Soens, B., Huber, M. S., McKibbin, S., van Ginneken, M., Debaille, V., Greenwood, R. C., Franchi, I. A., Cnudde, V., Van Malderen, S., Vanhaecke, F., Koeberl, C., Topa, D. & Claeys, P. (2019). *Geochim. Cosmochim. Acta.* Submitted.

Grieten, E., Schalm, O., Tack, P., Bauters, S., Storme, P., Gauquelin, N., Caen, J., Patelli, A., Vincze, L. & Schryvers, D. (2017). *J. Cult. Herit.* **28**, 56–64.

Jochum, K. P., Dingwell, D. B., Rocholl, A., Stoll, B., Hofmann, A. W., Becker, S., Besmehn, A., Bessette, D., Dietze, H. J., Dulski, P., Erzinger, J., Hellebrand, E., Hoppe, P., Horn, I., Janssens, K., Jenner, G. A., Klein, M., McDonough, W. F., Maetz, M., Mezger, K., Müker, C., Nikogosian, I. K., Pickhardt, C., Raczek, I., Rhede, D., Seufert, H. M., Simakin, S. G., Sobolev, A. V., Spettel, B., Straub, S., Vincze, L., Wallianos, A., Weckwerth, G., Weyer, S., Wolf, D. & Zimmer, M. (2000). *Geostand. Geoanal. Res.* **24**, 87–133.

Love, S. G. & Brownlee, D. E. (1993). *Science*, **262**, 550–553.

Monico, L., Janssens, K., Alfeld, M., Cotte, M., Vanmeert, F., Ryan, C. G., Falkenberg, G., Howard, D. L., Brunetti, B. G. & Miliani, C. (2015). *J. Anal. At. Spectrom.* **30**, 613–626.

Niekerk, D. van, Greenwood, R. C. & Franchi, I. A. (2007). *70th Annual Meteoritical Society Meeting*, 13–17 August 2007, Tucson, Arizona, USA, p. 5196.

Noguchi, T., Nakamura, T. & Nozaki, W. (2002). *Earth Planet. Sci. Lett.* **202**, 229–246.

Rochette, P., Folco, L., Suavet, C., van Ginneken, M., Gattacceca, J., Perchiazzi, N., Braucher, R. & Harvey, R. P. (2008). *Proc. Natl Acad. Sci. USA*, **105**, 18206–18211.

Rubin, A. E. (2018). *Meteorit. Planet. Sci.* **53**, 2181–2192.

Rubin, A. E. & Grossman, J. N. (2010). *Meteorit. Planet. Sci.* **45**, 114–122.

Salomé, M., Cotte, M., Baker, R., Barrett, R., Benseny-Cases, N., Berruyer, G., Bugnazet, D., Castillo-Michel, H., Cornu, C., Fayard, B., Gagliardini, E., Hino, R., Morse, J., Papillon, E., Pouyet, E., Rivard, C., Solé, V. A., Susini, J. & Veronesi, G. (2013). *J. Phys. Conf. Ser.* **425**, 182004–182007.

Schalm, O., Crabbé, A., Storme, P., Wiesinger, R., Gambirasi, A., Grieten, E., Tack, P., Bauters, S., Kleber, C., Favaro, M., Schryvers, D., Vincze, L., Terryn, H. & Patelli, A. (2016). *Appl. Phys. A*, **122**, 903.

Suavet, C., Rochette, P., Kars, M., Gattacceca, J., Folco, L. & Harvey, R. P. (2009). *Polar Sci.* **3**, 100–109.

Tack, P., Cotte, M., Bauters, S., Brun, E., Banerjee, D., Bras, W., Ferrero, C., Delattre, D., Mocella, V. & Vincze, L. (2016). *Sci. Rep.* **6**, 20763.

Tack, P., Garrevoet, J., Bauters, S., Vekemans, B., Laforce, B., Van Ranst, E., Banerjee, D., Longo, A., Bras, W. & Vincze, L. (2014). *Anal. Chem.* **86**, 8791–8797.

Tack, P., Vekemans, B., Laforce, B., Rudloff-Grund, J., Hernández, W. Y., Garrevoet, J., Falkenberg, G., Brenker, F. E., Van Der Voort, P. & Vincze, L. (2017). *Anal. Chem.* **89**, 2123–2130.

Tarduno, J. A., Cottrell, R. D., Nimmo, F., Hopkins, J., Voronov, J., Erickson, A., Blackman, E., Scott, E. R. & McKinley, R. (2012). *Science*, **338**, 939–942.

Vanmeert, F., Van der Snickt, G. & Janssens, K. (2015). *Angew. Chem. Int. Ed.* **54**, 3607–3610.

Vekemans, B., Janssens, K., Vincze, L., Adams, F. & Van Espen, P. (1994). *X-ray Spectrom.* **23**, 278–285.

Wasson, J. T. & Choi, B. G. (2003). *Geochim. Cosmochim. Acta*, **67**, 3079–3096.